Image Based Iterative Active Error Compensation for Polygon Mirror Based Scanning Systems

Bo Cong, Han Woong Yoo, and Georg Schitter

***Abstract*—This paper deals with the correction of cross-scan errors in polygon mirror (PM)-based laser scanning systems by active error compensation (AEC) using a fast-steering mirror (FSM). However, AEC is susceptible to sensor non-collocation errors since the FSM is typically controlled via an internal angular sensor. This sensor error can be evaluated by position measurements of the scanning laser, but these measurements are not always feasible due to the inherent duty cycle of PM-based scanning systems. Image-based iterative AEC (II-AEC) is proposed to use partial measurements to address the sensor non-collocation error, thereby improving the precision of PM-based scanning systems. II-AEC consists of a cascade structure where the inner loop employs iterative learning control for the FSM using the internal sensor, and the outer loop iterates the inner-loop reference based on the laser positions measured by a CMOS sensor. II-AEC has been implemented and evaluated on a PM-based stereolithography apparatus, resulting in a 40-fold printing precision improvement compared to the uncompensated apparatus.**

***Index Terms*—Fast Steering Mirror, Polygon Mirror, Error Compensation, Image-based Control, Iterative Learning Control**

I. Introduction

POLYGON mirror (PM)-based scanning systems are subject to repetitive cross-scan errors that limit their scanning precision, but these errors can be mitigated through active error compensation (AEC) using a fast-steering mirror (FSM) [1]–[3]. Due to facet tilts of the PM, the scanning system deflects the laser beam in the direction orthogonal to the main scan axis by up to hundreds of microradians, resulting in repetitive cross-scan errors with each revolution [1]. By pre-directing the laser beam for each facet during the scan, an FSM can compensate for the tilt difference of each facet. FSMs are typically chosen because of their fast dynamic response in small angle ranges [3], e.g., a few degrees or less [4], in comparison to galvanometer scanners, which are often used for scanning over tens of degrees [5]. With advanced control strategies, such as iterative learning control (ILC), an FSM can track a fast-varying compensation trajectory without compromising tracking accuracy. The ILC-based AEC (ILC-AEC) achieves a 27-fold error reduction [2], [6]. Using FSM to manipulate laser beam path with microradian accuracy is also widely applied in fields such as space communication [7], image motion compensation [8], image scanning [9].

The authors are with the Mechatronics and Power Electronics Institute (MPEI), TU Wien, 1040 Vienna. Corresponding author: bo.cong@tuwien.ac.at.

Manuscript received xx xxxx 2025; revised xx xxxx 2025; accepted xx xxxx 2025.

FSMs are typically equipped with internal angular sensors to establish a closed-loop control system for accurate mirror angle control [10]–[12]. A high-bandwidth closed-loop control design improves the tracking accuracy of FSMs to a dynamic reference, but the improvement is constrained by causality [12]. In special cases where the reference is repetitive, ILC can be used to further reduce the tracking error [6], [13]. Despite advanced control methods, the control loop based on the internal sensor cannot guarantee the performance of the FSM due to "dynamic deviations", arising from the non-collocation between the internal sensor and the mirror [11], [14]. Besides the low-pass characteristics of sensor electronics, this dynamic deviation is typically caused by structural modes of the mirror assembly [11], [15], [16]. As the structural modes are typically situated at high frequencies, the dynamic deviation is more noticeable when driving the FSM with a fast reference, such as in AEC for PM-based scanning systems [2].

Model-based and measurement-based solutions have been proposed in the literature to address this challenge. In [15], the inverted sensor model is incorporated as an additional transformation in the control loop for a galvanometer scanner, improving the angle tracking accuracy by a factor of 7.5; however, the improvement relies on the accuracy of the sensor model. Measurement-based approaches aim to directly assess the tracking accuracy using beam position measurements on the target plane [7], [17], [18], achieving sub-microradian precision in space communication applications [17].

Both position-sensitive devices (PSDs) and CMOS sensors are widely used for laser beam position measurements [19], [20]. PSDs convert beam position into electrical signals with bandwidths above 10 kHz bandwidth [19], but lack beam intensity and spatial distribution data often needed for scanning system evaluation [21], [22]. CMOS sensors capture the beam profile and determine position via post-processing, achieving spatial precision of one-tenth of a pixel [23] or an optical angular resolution of 0.13 µrad for mirror tilt [24]. A global shutter is preferred, as rolling-shutter CMOS sensors may introduce distortions when measuring moving laser beams. While limited by frame rate and processing time in real-time use [19], CMOS sensors are well suited for offline measurements. Combined with linear stages, CMOS sensors enable meter-scale offline beam position measurements, making them suitable for evaluating PM-based scanners [2].

Using image-based control to improve trajectory tracking accuracy is also known as visual servoing in robotics and automation systems [25], [26]. The tracking error of, for instance,

Pre-print version of the article: B. Cong, Han Woong Yoo and G. Schitter, "Image Based Iterative Active Error Compensation for Polygon Mirror Based Scanning Systems," *IEEE/ASME Transactions on Mechatronics*pp. 1-12, 2026. DOI: 10.1109/TMECH.2026.3651912

a robot manipulator is computed from the captured images by a camera mounted on the robot arm or at fixed positions, and fed back to the robot joint actuation to correct local sensor errors [26]. Offline measurements based on captured images can also be incorporated into ILC frameworks for robotics to improve tracking accuracy [27]. Image-based control is also applicable to other performance aspects, such as extrusion accuracy in micro-robotic deposition [28] and layer shape control in micro-stereolithography [29].

Image-based control within the ILC framework has the potential to resolve the sensor non-collocation error in AEC; however, the duty cycle of PM-based scanning systems must also be addressed. These scanning systems correlate the laser beam direction to the laser position only within a limited portion of the total scan angle, defined by the duty cycle [1], [2]. Outside this duty cycle, the integrity of the laser beam is compromised. Consequently, measuring the laser position on the target plane provides only a partial evaluation of the FSM dynamics. Data unavailability in the ILC framework has been investigated in the context of networked systems [30], [31], where random dropout is assumed at each time step during the repetition period. However, this assumption is not applicable to the AEC, where data dropout is dictated by the duty cycle and follows a deterministic binary pattern.

This paper makes the following key contributions:

i) A new image-based iterative active error compensation (II-AEC) scheme for PM-based scanning systems, which uses cascade ILC together with image-based laser position measurements to compensate dynamic errors arising from FSM-sensor non-collocation.
ii) A general design methodology for selecting the learning and update filters within the cascade ILC framework, ensuring stable learning and improved error reduction.
iii) An experimental demonstration on a PM-based stereolithography apparatus confirming the effectiveness of the proposed approach.

The rest of this article is organized as follows. In Section II the principle of AEC in a PM-based scanning system is introduced, and the sensor non-collocation of the FSM is analyzed. Section III introduces the proposed II-AEC method, which is implemented and experimentally evaluated in Section IV. Lastly, Section V concludes the paper.

II. Active Error Compensation with FSM

A. System description

A high-speed, high-resolution, and large-scale PM-based stereolithography apparatus (SLA) is used in this paper to demonstrate AEC for cross-scan errors using an FSM [2]. This SLA consists of a rigidly integrated PM-based scanner and measurement stage, as shown in Fig. 1.

The PM-based scanner delivers and focuses laser beams to a defined print plane by an 8-facet PM and an F-Theta lens. Laser beams are directed onto the PM facet by an FSM. Each facet of the PM scans the laser beam to print a single line in each PM revolution in a consecutive manner. The scan lines are evaluated by a CMOS sensor (3.75 µm × 3.75 µm pixel size) mounted on an X-Y stage assembly positioned on the print plane of the scanner. More details on the used hardware can be found in authors' previous work [2].

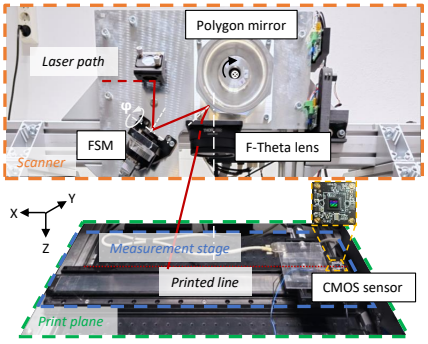

Fig. 1. PM-based scanning system with AEC. The system consists primarily of an 8-facet PM, a long-focus F-Theta lens, and a 405-nm laser achieving a scan speed of 230 m/s over a ±0.23 m scan range (or ±22° optically) with an FWHM spot size of 22 µm [2]. An FSM is employed to implement AEC for cross-scan errors, improving the printing precision. The cross-scan error of the scanner is evaluated by the measurement stage, using a linear stage assembly and a CMOS sensor. The X, Y, and Z coordinates are defined by the nominal scan direction, the PM rotation axis, and the right-hand rule, respectively.

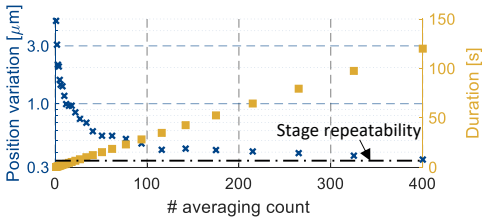

Fig. 2. Scan line position variation from 20 repeated measurements of Facet 1 at the center of the scan range using the CMOS sensor and linear stage. Left: variation decreases with increased averaging of captures but is limited by stage repeatability. Right: estimated measurement duration increases linearly with the averaging counts.

The CMOS sensor captures segments of continuous scan lines, with its shutter synchronized to the PM rotation. Moving the CMOS sensor with the X-stage over a 0.5 m stroke enables full coverage of the designed scan range. The captured images reveal the laser beam's intensity profile, and beam positions are extracted by combining image data with linear stage positions [2]. Averaging multiple image captures is employed to robustly extract the deterministic scan-line position from non-deterministic disturbances in the PM-based scanning system, including vibrations and wind disturbances. Measurement accuracy is additionally constrained by the linear stage repeatability [32]. Fig. 2 presents the variation in the scan line position from repeated measurements using different numbers of captures for averaging. An averaging count of 100 captures provides a measure precision of 0.5 µm and is used as a trade-off against measurement duration. The CMOS sensor orientations and linear stage errors are calibrated to the nominal scan direction (X-axis), defined by the average orientation of scan lines generated across all facets of the PM.

By moving the Y-stage at a constant speed, the print references are shifted by a distance d_{L-L} on the print plane,

Pre-print version of the article: B. Cong, Han Woong Yoo and G. Schitter, "Image Based Iterative Active Error Compensation for Polygon Mirror Based Scanning Systems," *IEEE/ASME Transactions on Mechatronics*pp. 1-12, 2026. DOI: 10.1109/TMECH.2026.3651912

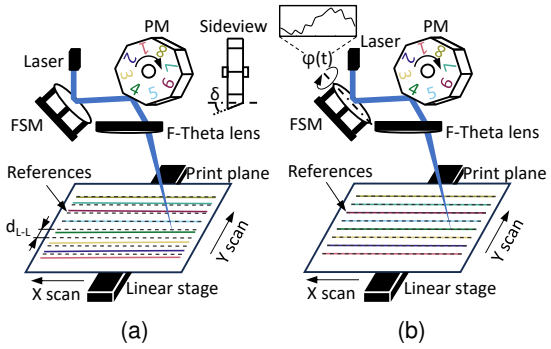

Fig. 3. PM-based scanning system achieves raster scanning by synchronizing linear stage motion with PM rotation. (a) Facet tilts in the PM introduce print errors, causing the printed lines to deviate from their reference positions in the cross-scan direction. (b) An FSM is employed to actively compensate for the cross-scan error by steering the laser beam with an angle $\varphi(t)$.

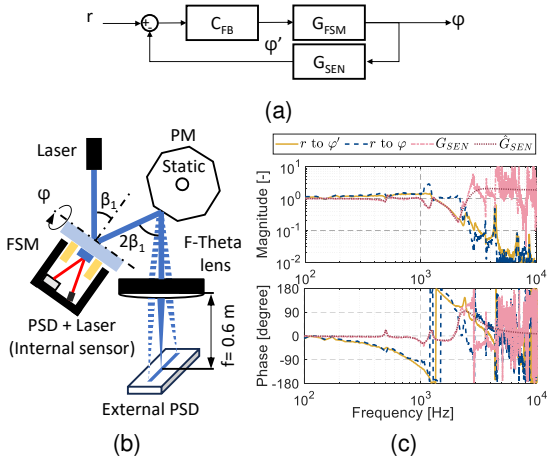

Fig. 4. Internal angular sensor dynamics. (a) G_{SEN} is demonstrated in the closed-loop controlled FSM. (b) An external PSD measures the actual angle φ, which is compared against the internal sensor measurement φ'. (c) Frequency response functions of the closed-loop FSM are identified with the internal PSD (solid yellow) and the external PSD (dashed blue). The identified G_{SEN} (dash-dotted light red) is estimated by a parametric model $\hat{G}_{SEN}$ (dotted dark red).

resulting in a raster print pattern as shown in Fig. 3. Due to PM facet tilts δ, deterministic cross-scan errors arise in the PM-based scanning system [33], causing scan lines to deviate from the reference, as illustrated in Fig. 3(a). To reduce this error, AEC is implemented using the FSM, which steers the laser beam via an angle $\varphi(t)$, as shown in Fig. 3(b). PM facet imperfections in the X-Z plane create so-called facet-to-facet errors, which can be largely eliminated using start-of-scan sensors [1], [6], and have negligible impact on the AEC [2].

The scanner and measurement stage are interfaced and controlled via a rapid prototyping system (DS1005, dSPACE GmbH, Germany), operating at a sampling rate of 20 kHz.

B. Sensor non-collocation

The FSM achieves AEC by tip-tilting the mirror according to a trajectory r, typically within 1 mrad. An internal angular sensor is used to implement feedback (FB) control of the mirror angle φ to ensure steering accuracy. However, since the angular sensor is not located directly on the mirror surface, it is non-collocated with the actual mirror angle. This non-collocation can lead to a dynamic mismatch between the measured and actual mirror angles, denoted by φ' and φ, respectively. This dynamic mismatch is represented by internal sensor dynamics G_{SEN} in the block diagram, shown in Fig. 4(a). The FSM plant and the FB controller in the closed-loop system are represented by G_{FSM} and C_{FB}, respectively. Since the closed-loop transfer functions from r to φ' and φ are derived as

$$T_{r\to\varphi'} = \frac{G_{SEN}\, G_{FSM}\, C_{FB}}{1 + G_{SEN}\, G_{FSM}\, C_{FB}}, \tag{1}$$

and

$$T_{r\to\varphi} = \frac{G_{FSM}\, C_{FB}}{1 + G_{SEN}\, G_{FSM}\, C_{FB}}. \tag{2}$$

respectively, the internal sensor dynamics can be identified from

$$G_{SEN} = T_{r\to\varphi}^{-1}\, T_{r\to\varphi'}. \tag{3}$$

In addition to the internal sensor dynamics, misalignment between the pivot point and the laser beam is another common deterministic source of beam steering errors, as FSM rotation induces a lateral shift of the laser beam. However, this beam shift is translational and can be considered negligible in the present scanning system for two reasons: (1) the FSM only rotates less than 1 mrad, resulting in lateral displacements on nanometer scale, and (2) the optical system, including the F-Theta lens, is largely insensitive to such lateral shifts [34].

The considered FSM employs an internal optical sensor to achieve closed-loop control, and the concept is demonstrated in Fig. 4(b). The PSD measures the assistant laser beam after being reflected by the ancillary mirror, providing an angle evaluation φ' for the FSM. Similarly, an external PSD can be configured to directly evaluate the actual angle of the mirror φ, revealing the internal sensor dynamics G_{SEN}.

Fig. 4(b) shows a one-degree PSD (1L30UVSU2, SiTek Electro Optics AB, Sweden) is placed at the center of the print plane and aligned with the Y-axis to evaluate φ of the FSM. With the PM held static, the cross-scan displacement y of the laser beam on the print plane serves as a measure of the actual FSM angle φ. The exact correlation between y and φ can be derived from [35], and here a linear approximation

$$y \approx 2f\, \varphi\, \cos\beta_1 \tag{4}$$

is used, where f is the focal length of the F-Theta lens, and β_1 is the beam's incident angle on the FSM in the X-Z plane. This approximation error is less than one part per million (1 ppm) for $\varphi < \pm 1$ mrad.

The frequency response functions (FRFs) of the transfer functions $T_{r\to\varphi'}$ and $T_{r\to\varphi}$ are identified using white-noise references and are plotted in Fig. 4(c). The internal sensor dynamics G_{SEN}, derived from (3), are represented by the dash-dotted light red line in Fig. 4(c). Multiple zero-pole doublets are visible in G_{SEN} from approximately 500 Hz, indicating that small masses decoupled from the mirror [11]. Sensor

Pre-print version of the article: B. Cong, Han Woong Yoo and G. Schitter, "Image Based Iterative Active Error Compensation for Polygon Mirror Based Scanning Systems," *IEEE/ASME Transactions on Mechatronics*pp. 1-12, 2026. DOI: 10.1109/TMECH.2026.3651912

dynamics in internal FSM sensors, similar to those observed here, have also been reported in [14] and characterized using pole-zero doublet models in [11]. Here, a parametric model

$$\hat{G}_{SEN} = k_{sen} \prod_{i=1}^{4} \frac{s^2 + \zeta_i\, z_i\, s + z_i^2}{s^2 + \rho_i\, p_i\, s + p_i^2} \tag{5}$$

is derived to describe the internal sensor dynamics G_{SEN} up to 2500 Hz, and consists of four zero-pole doublets and a gain factor $k_{sen} = 1.8$. The parameters of these doublets are listed in Tab. I.

TABLE I
ZERO-POLE DOUBLETS OF INTERNAL SENSOR

i	1	2	3	4
ζ_i	0.04	0.22	0.09	0.12
z_i	1005π	2121π	2429π	4192π
ρ_i	0.04	0.18	0.08	0.57
p_i	1015π	2040π	2515π	5618π

The internal sensor dynamics resulting from the non-collocation between the sensor and the mirror lead to a deviation between the measured and actual angle. In particular, when the AEC demands a fast trajectory r that contains frequency components near or above 500 Hz, the achievable compensation accuracy becomes limited.

C. Mapping angle to position with duty cycle

Measuring the actual FSM angle φ helps resolve the sensor non-collocation error in the AEC. Since the FSM angle φ is reflected in the cross-scan position of scan lines on the print plane, line position measurements obtained via CMOS sensors can be used to assess the FSM angle.

The FSM angle φ is mapped to the scan line position (x, y) [35]. For $\varphi < \pm 1$ mrad, linear approximations can be applied to simplify the correlation between y and φ to θ-dependent gains

$$y \approx K_{\varphi\to y}(\theta)\,\varphi \quad \text{and} \quad \varphi \approx K_{y\to\varphi}(\theta)\,y, \tag{6}$$

where θ is the rotation angle of the PM. The x position becomes a function of θ only. In practice, this function is calibrated by correlating the laser modulation time, the PM encoder readout, and the captured laser position from the measurement stage. The error introduced by this simplification is less than 1 ppm within an optical scan angle of $\pm 22°$. Given the constant rotational speed of the PM, denoted by ω_{PM}, the gains $K_{\varphi\to y}$ and $K_{y\to\varphi}$ are time-dependent.

The mapping between φ and y, however, can only be established within the duty cycle of PM-based scanning systems due to optical constraints [1], [2]. For a N_f-facet PM-based scanning system of a duty cycle μ, the laser beam is only projected when the rotation angle satisfies

$$\theta_{on} = \left\{ \theta \in \mathbb{R} \mid \theta_f \le \theta \le \theta_f + \mu \frac{2\pi}{N_f} \right\}, \tag{7}$$

and turned off when

$$\theta_{off} = \left\{ \theta \in \mathbb{R} \mid \theta_f + \mu \frac{2\pi}{N_f} < \theta < \theta_f + \frac{2\pi}{N_f} \right\}. \tag{8}$$

The angle θ_f is defined for each facet of the PM

$$\theta_f(i) = (i-1)\,\frac{2\pi}{N_f}, \quad i = \{1, 2, \cdots, N_f\}. \tag{9}$$

Plugging in the PM rotational speed ω_{PM}, the angle sections (7) and (8) define piecewise-defined temporal windows

$$t_{on} = \frac{\theta_{on}}{\omega_{PM}} \quad \text{and} \quad t_{off} = \frac{\theta_{off}}{\omega_{PM}}. \tag{10}$$

The union of these two windows constitutes a full PM repetition period, $t_{PM} = t_{on} \cup t_{off}$. The correlation (6) is valid only within the scanning window t_{on} and does not hold during the transition window t_{off}.

By accounting for the time-varying gain and the duty cycle of the PM-based scanning system, only a partial evaluation of the FSM angle is feasible using image-based measurements. Consequently, integrating image-based measurements into the AEC introduces nonlinearity into the FSM control.

III. IMAGE BASED ITERATIVE AEC

Image-based iterative AEC (II-AEC) is proposed to address the sensor non-collocation error of the FSM in the AEC, thereby reducing cross-scan errors in PM-based scanning systems. The II-AEC adopts a cascade iterative learning structure, in which the learning and updating filters are specifically designed to accommodate the nonlinearity introduced by the image-based measurements.

A. Control structure

Fig. 5 illustrates the proposed control structure for the II-AEC, implemented in a cascade configuration. The inner loop incorporates the modeled internal sensor dynamics $\hat{G}_{SEN}$ and the FSM dynamics with ILC. In the outer loop, the learning filter L_{OUT} maps the measured laser positions to the FSM angles φ, while the updating filter Q_{OUT} ensures learning convergence of the cascade loops. The implementation procedure is detailed in Algorithm 1.

The algorithm starts by setting the initial compensation trajectory r^0 to zero, and measuring the uncompensated cross-scan error Δy^0 using the CMOS sensor. This error is then mapped to the scanning window t_{on} based on the established correlation between scan position x and PM rotation angle θ. To provide an effective initial guess for the compensation trajectory during the transition window t_{off}, the product $L_{OUT}\,\Delta y^0$ is interpolated over a full PM repetition period t_{PM} using MATLAB's "interp1" function with the "spline" method. This interpolation yields a smooth trajectory and helps reduce the number of required learning iterations. In each outer-loop iteration n, the current trajectory r^n is filtered through the internal sensor model $\hat{G}_{SEN}$, producing the FSM control reference r'. This reference is then tracked in the inner loop using FB control and ILC, based on the FSM's internal sensor. After N_m inner-loop iterations, the final feedforward signal f^{N_m} is retained as the input f for FSM actuation. The CMOS sensor is again used to measure the residual cross-scan error Δy^n, which is then processed by the outer-loop learning filter L_{OUT} and updating filter Q_{OUT} to generate

Pre-print version of the article: B. Cong, Han Woong Yoo and G. Schitter, "Image Based Iterative Active Error Compensation for Polygon Mirror Based Scanning Systems," *IEEE/ASME Transactions on Mechatronics*pp. 1-12, 2026. DOI: 10.1109/TMECH.2026.3651912

Algorithm 1 Image-based iterative AEC

Input: Controller C_{FB}, sensor model $\hat{G}_{SEN}$, learning filters L_{IN} and L_{OUT}, updating filters Q_{IN} and Q_{OUT}, and iterations N_m and N_n.
Output: Compensation trajectory r, FSM reference r' and feedforward signal f.

Initialize outer loop: $n \leftarrow 0$, $r^0 \leftarrow 0$
for all $n = 0$ to N_n **do**
  Initialize inner loop: $r' \leftarrow \hat{G}_{SEN}\, r^n$, $m \leftarrow 0$, $f^0 \leftarrow 0$
  for all $m = 0$ to N_m **do**
    Measure tracking error e^m of FSM
    $f^{m+1} \leftarrow Q_{IN}\,(f^m + L_{IN}\, e^m)$
  end for
  Keep feedforward signal $f \leftarrow f^{N_m}$
  Measure scan line position $(x, \Delta y^n)$ using CMOS sensor and linear stages; map measurement to t_{on}
  if $n = 0$ **then**
    $r^1 \leftarrow Q_{OUT}\,(r^0 - \text{interp1}\,(t_{on}, L_{OUT}\,\Delta y^0, t_{PM}))$
  else
    $r^{n+1} \leftarrow Q_{OUT}\,(r^n - L_{OUT}\,\Delta y^n)$
  end if
end for
Keep trajectory $r \leftarrow r^{N_n}$ and reference $r' \leftarrow \hat{G}_{SEN} r^{N_n}$
Return r, r' and f

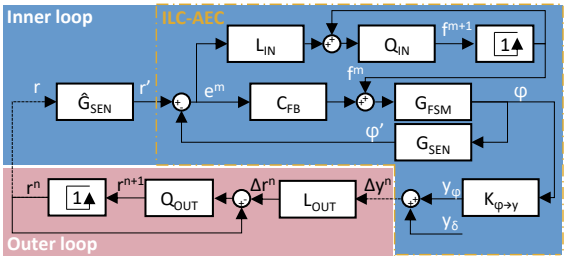

Fig. 5. II-AEC for PM-based scanning systems is designed in a cascade structure with two iteration loops. The inner loop (blue background) ensures accurate tracking of the FSM angle φ to the compensation trajectory r. The outer loop (pink background) updates the compensation trajectory r^n iteratively using image-based measurements of the cross-scan error Δy^n. The learning and updating filters are denoted by L and Q, with subscripts $(\cdot)_{IN}$ and $(\cdot)_{OUT}$ specifying the inner and outer loops, respectively. The diagram enclosed by the yellow dash-dotted line depicts the ILC-AEC approach [2], which includes only the inner ILC loop.

the next compensation trajectory r^{n+1}. This process repeats for N_n outer-loop iterations, after which the final trajectory r^{N_n} is adopted as the compensation trajectory r, and the corresponding filtered reference $r' = \hat{G}_{SEN} r^{N_n}$ is used for the FSM control. The values of N_n and N_m are user-defined parameters selected to ensure that learning in the outer and inner loops continues until convergence.

The inner-loop learning and updating filters are adopted from typical ILC designs [2]

$$L_{IN} = \hat{P}^{-1} \quad \text{and} \quad Q_{IN} = F_{BW}(f_{in})\, F^*_{BW}(f_{in}), \tag{11}$$

where F_{BW} and F^*_{BW} are a complex conjugate pair of Butterworth filters with a cut-off frequency f_{in} =2 kHz, ensuring the convergence of the inner loop. The learning filter is derived from the modeled process sensitivity of the FSM

$$\hat{P}(s) = \hat{G}_{FSM}\left(1 + \hat{G}_{FSM}\, C_{FB}\right)^{-1}. \tag{12}$$

The FSM plant model $\hat{G}_{FSM}$ and the FB controller C_{FB} of the considered FSM are [2]

$$\hat{G}_{FSM}(s) = \frac{\omega_0^2}{s^2 + 0.08\omega_0\, s + \omega_0^2} e^{-s\, t_d} \tag{13}$$

and

$$C_{FB}(s) = k_p \left(1 + \frac{k_i}{s} + \frac{k_d\, s}{k_n\, s + 1}\right) \frac{\omega_{lp}^2}{s^2 + 0.8\omega_{lp}\, s + \omega_{lp}^2}, \tag{14}$$

respectively, with the parameters given in Tab. II.

TABLE II
PARAMETERS OF FSM MODEL AND FB CONTROLLER

ω_0	t_d	k_p	k_i	k_d	k_n	ω_{lp}
169.6 rad/s	25 µs	90	10	0.0016	8×10^{-6}	$4800\,\pi$ rad/s

For the outer loop, the learning filter is defined by the correction sensitivity of the cross-scan error

$$L_{OUT} = K_{y\to\varphi}, \tag{15}$$

which, when combined with the projection sensitivity $K_{\varphi\to y}$ in the cascade structure, ideally yields a constant overall gain. For the outer-loop updating filter, a fourth-order zero-phase Butterworth filter

$$Q_{OUT} = F_{BW}(f_{out})\, F^*_{BW}(f_{out}) \tag{16}$$

is considered, with the cut-off frequency f_{out} being a tunable parameter. The choice of f_{out} has to balance the learning convergence and performance of the cascade loop.

B. System dynamics and lifted system representation

The cascade loop is formulated using lifted system representations to facilitate the filter design and implementation. With a constant rotational speed ω_{PM} of the PM and a fixed digital sampling time t_s, the FSM dynamics in lifted form have a finite length N, which corresponds to the PM repetition period. The dynamics are expressed in matrix form [36] as

$$\Phi = \mathcal{J}\, R, \tag{17}$$

where the output angle vector $\Phi = [\varphi(0), \varphi(1), \cdots, \varphi(N-1)]^\top$ and the trajectory vector $R = [r(0), r(1), \cdots, r(N-1)]^\top$ each represent the system states sampled at discrete time points within one repetition period N. The FSM dynamic $\mathcal{J}$ is a circulant matrix of the form

$$\mathcal{J} = \begin{bmatrix} H(0) & H(N-1) & \dots & H(1) \\ H(1) & H(0) & \dots & H(2) \\ \vdots & \vdots & \ddots & \vdots \\ H(N-1) & H(N-2) & \dots & H(0) \end{bmatrix}, \tag{18}$$

where each column is constructed from the system response function $H(k)$, which satisfies the periodicity condition

$$H(k) = H(k + aN),\ a \in \mathbb{N}_0,\ k \in \{0, 1, \cdots, N-1\}. \tag{19}$$

Pre-print version of the article: B. Cong, Han Woong Yoo and G. Schitter, "Image Based Iterative Active Error Compensation for Polygon Mirror Based Scanning Systems," *IEEE/ASME Transactions on Mechatronics*pp. 1-12, 2026. DOI: 10.1109/TMECH.2026.3651912

For a repetitive linear system, $\mathcal{J}$ can be derived directly from the FRF using the decomposition [36], [37]

$$\mathcal{J} = \mathcal{U}\,\Lambda\,\mathcal{U}^*, \tag{20}$$

where $(\cdot)^*$ denotes the conjugate transpose. The transformation matrix $\mathcal{U}$ is unitary and is defined as

$$\mathcal{U} = \frac{1}{\sqrt{N}}\begin{bmatrix} M_0 & M_1 & \cdots & M_{N-1}\end{bmatrix}, \tag{21}$$

with

$$M_k = \begin{bmatrix} e^{-0j\omega_k t_s} & e^{-1j\omega_k t_s} & \cdots & e^{-(N-1)j\omega_k t_s}\end{bmatrix}^\top \tag{22}$$

representing the k^{th} eigenvector of $\mathcal{J}$ at the frequency $\omega_k = 2\pi\frac{k}{Nt_s}$. The eigenvalue matrix Λ is a diagonal matrix that contains the discrete Fourier transform representation of the FSM dynamics:

$$\Lambda = \operatorname{diag}\left(\begin{bmatrix}\lambda_0 & \lambda_1 & \cdots & \lambda_{N-1}\end{bmatrix}\right). \tag{23}$$

The overall FSM dynamics of the inner loop combine the sensor model $\hat{G}_{SEN}$, the sensor dynamics G_{SEN}, and the FSM control loop dynamics $\bar{G}_{FSM}$, and are expressed as

$$\varphi = G_{SEN}^{-1}\,\bar{G}_{FSM}\,\hat{G}_{SEN} r. \tag{24}$$

Here, $\bar{G}_{FSM}$ represents the equivalent FSM system dynamic after convergence of the inner-loop ILC, estimated as follows:

$$\bar{G}_{FSM} = 1 - (1 - Q_{IN}\,(1 - P\,L_{IN}))^{-1}\,(1 - Q_{IN})\,S, \tag{25}$$

where the sensitivity S and process sensitivity P of the closed-loop FSM are defined as

$$S = (1 + G_{SEN}\,G_{FSM}\,C_{FB})^{-1}, \tag{26}$$
$$P = G_{SEN}\,G_{FSM}S, \tag{27}$$

respectively. Consequently, the eigenvalues λ_k of $\mathcal{J}$ are computed as

$$\lambda_k = \begin{cases} G_{SEN}^{-1}(j\omega_k)\,\bar{G}_{FSM}(j\omega_k)\,\hat{G}_{SEN}(j\omega_k), & k \le \frac{N}{2} \\ \lambda_{N-k}^*, & k > \frac{N}{2}\end{cases}. \tag{28}$$

Fig. 6(a) and (c) visually illustrate the response function $H(k)$ and the circulant matrix $\mathcal{J}$, respectively, as derived from FRF identification. The inner-loop ILC ensures zero-phase delay in the FSM response to a repetitive trajectory.

Similarly, the outer-loop learning filter Q_{OUT} can be formulated as

$$\mathcal{Q}_{OUT} = \mathcal{U}\,\Lambda_Q\,\mathcal{U}^* \tag{29}$$

where Λ_Q is a diagonal matrix containing the frequency-domain representation of the filter.

Besides the dynamic system in the cascade loop, the time-varying gains $K_{\varphi\to y}$ and L_{OUT} are also reformulated in lifted representations. The PM duty cycle divides the repetition period into piecewise temporal windows t_{on} and t_{off}. Given the sampling time t_s, the corresponding sample indices for each window are defined as

$$k_{on} = \{k \in \{0, 1, \cdots, N-1\} \mid k\,t_s \in t_{on}\}, \tag{30}$$
$$k_{off} = \{k \in \{0, 1, \cdots, N-1\} \mid k\,t_s \in t_{off}\}. \tag{31}$$

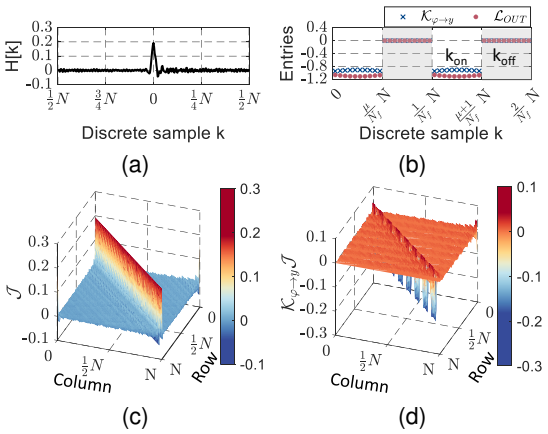

Fig. 6. System dynamics in lifted representations. (a) Response function $H(k)$ of the FSM dynamics, including the inner-loop ILC. (b) Diagonal entries of $\mathcal{K}_{\varphi\to y}$ and $\mathcal{L}_{OUT}$. (c) FSM dynamics in lifted representation $\mathcal{J}$ (d) Inner-loop dynamics represented as the product $\mathcal{K}_{y\to\varphi}\mathcal{J}$.

Since no correlation between y and φ exists at the sample indices k_{off}, (6) is specified as

$$y(k) = \begin{cases} K_{\varphi\to y}(\omega_{PM}\,k\,t_s)\,\varphi(k), & k \in k_{on} \\ 0, & k \in k_{off}\end{cases}, \tag{32}$$

$$\varphi(k) = \begin{cases} K_{y\to\varphi}(\omega_{PM}\,k\,t_s)\,y(k), & k \in k_{on} \\ 0, & k \in k_{off}\end{cases}. \tag{33}$$

Expressing these correlations in matrix form yields the projection matrix

$$Y_\varphi = \mathcal{K}_{\varphi\to y}\,\Phi, \tag{34}$$

and the learning filter matrix

$$\Delta R = \mathcal{L}_{OUT}\,\Delta Y = \mathcal{K}_{y\to\varphi}\,\Delta Y. \tag{35}$$

Fig. 6(b) illustrates the diagonal entries of both matrices.

Combining the FSM dynamics $\mathcal{J}$ with the projection matrix $\mathcal{K}_{y\to\varphi}$ results in the inner-loop dynamic

$$\Delta Y^n = \mathcal{K}_{\varphi\to y}\,\mathcal{J}\,R^n + Y_\delta, \tag{36}$$

as shown in Fig. 6(d). Adding the outer-loop filter matrices $\mathcal{Q}_{OUT}$ and $\mathcal{L}_{OUT}$ completes the cascade learning control, with the updating function defined as

$$R^{n+1} = \mathcal{Q}_{OUT}\,(R^n - \mathcal{L}_{OUT}\,\Delta Y^n). \tag{37}$$

C. Updating filter design ensuring learning convergence

For the cascade control system defined by (36) and (37), the updating filter $\mathcal{Q}_{OUT}$ of the outer learning loop still needs to be designed with an appropriate cut-off frequency f_{out} to ensure both learning convergence and performance.

Plugging the inner-loop dynamics (36) into the updating function (37) yields

$$R^{n+1} = \underbrace{\mathcal{Q}_{OUT}\,(I - \mathcal{L}_{OUT}\,\mathcal{K}_{\varphi\to y}\,\mathcal{J})}_{\mathcal{M}_{conv}}\,R^n - \mathcal{Q}_{OUT}\,\mathcal{L}_{OUT}\,Y_\delta. \tag{38}$$

Pre-print version of the article: B. Cong, Han Woong Yoo and G. Schitter, "Image Based Iterative Active Error Compensation for Polygon Mirror Based Scanning Systems," *IEEE/ASME Transactions on Mechatronics*pp. 1-12, 2026. DOI: 10.1109/TMECH.2026.3651912

The outer-loop learning control monotonically converges if the matrix $\mathcal{M}_{conv}$ satisfies [38]

$$\bar{\sigma}(\mathcal{M}_{conv}) < 1, \tag{39}$$

where $\bar{\sigma}(\cdot)$ computes the maximum singular value of a matrix. By substituting (29) for $\mathcal{Q}_{OUT}$, the convergence matrix can be rewritten as

$$\mathcal{M}_{conv} = \mathcal{U}\,\Lambda_Q \left(I - \underbrace{\mathcal{U}^*\,\mathcal{L}_{OUT}\,\mathcal{K}_{\varphi\to y}\,\mathcal{U}}_{\Lambda_M}\,\Lambda \right) \mathcal{U}^*, \tag{40}$$

and the learning performance after convergence is estimated by

$$\Delta Y^{\infty} = \left(-\mathcal{K}_{\varphi\to y}\,\mathcal{J}\,\left(I - \mathcal{M}_{conv}\right)^{-1}\,\mathcal{Q}_{OUT}\,\mathcal{L}_{OUT} + I \right) Y_{\delta}. \tag{41}$$

Under the hypothetical condition of a 100% duty cycle ($\mu = 1$) for the PM-based scanning system, the mapping matrix Λ_M becomes the identity matrix. Thus, the convergence matrix (40) simplifies to

$$\mathcal{M}_{conv} = \mathcal{U}\,\Lambda_Q\,\left(I - \Lambda\right)\,\mathcal{U}^*, \tag{42}$$

and the monotonic convergence condition (39) is equivalent to requiring the maximum absolute value of the diagonal entries of $\Lambda_Q\,(I - \Lambda)$ to be less than one. Since $\mathcal{U}$ links each diagonal entry to frequency ω_k, this condition (42) is identical to the frequency-domain convergence condition [39]

$$\| Q_{OUT}\,\left(1 - G_{SEN}^{-1}\,\bar{G}_{FSM}\,\hat{G}_{SEN}\right) \|_{\infty} < 1. \tag{43}$$

For an ideal inner loop where $\Lambda = I$, (39) is trivially satisfied, and the learning performance depends solely on the updating filter $\mathcal{Q}_{OUT}$ as (41) reduces to

$$\Delta Y^{\infty} = \left(-\mathcal{K}_{\varphi\to y}\,\mathcal{Q}_{OUT}\,\mathcal{L}_{OUT} + I \right)\,Y_{\delta}. \tag{44}$$

Increasing the cut-off frequency f_{out} of Q_{OUT} enables a greater reduction in the cross-scan error ΔY. However, when the inner-loop dynamics are non-ideal ($\Lambda \neq I$), the bandwidth of Q_{OUT} is constrained by (39).

Fig. 7(a) shows the singular values of $\mathcal{M}_{conv}$ for $\mu = 1$, calculated from the diagonal entries of $\Lambda_Q\,(I - \Lambda)$, where Q_{OUT} has a cut-off frequency $f_{out} = 3.3$ kHz to satisfy (39). Plugging in the system parameters $t_s = 5 \times 10^{-5}$ s, $N = 320$, and $N_f = 8$ of the PM-based SLA, each singular value is mapped to a frequency ω_k, indicated on the horizontal axis of Fig. 7(a). This outer-loop learning bandwidth is fundamentally limited by the model accuracy of the FSM sensor dynamics, as significant phase discrepancies occur above about 3 kHz.

For a typical PM-based scanning system with $\mu < 1$, i.e., the FSM dynamics are only partially measured by the laser position measurement, the direct frequency-domain interpretation of (40) is no longer valid. The mapping matrix Λ_M becomes circulant, rather than diagonal, with each column's elements described by

$$H_M(k) = \frac{1}{N}\sum_{b=0}^{N-1} h_b\, e^{j\frac{2\pi\, b}{N}k},\; h_b = \begin{cases} 1, & b \in k_{on} \\ 0, & b \in k_{off} \end{cases}. \tag{45}$$

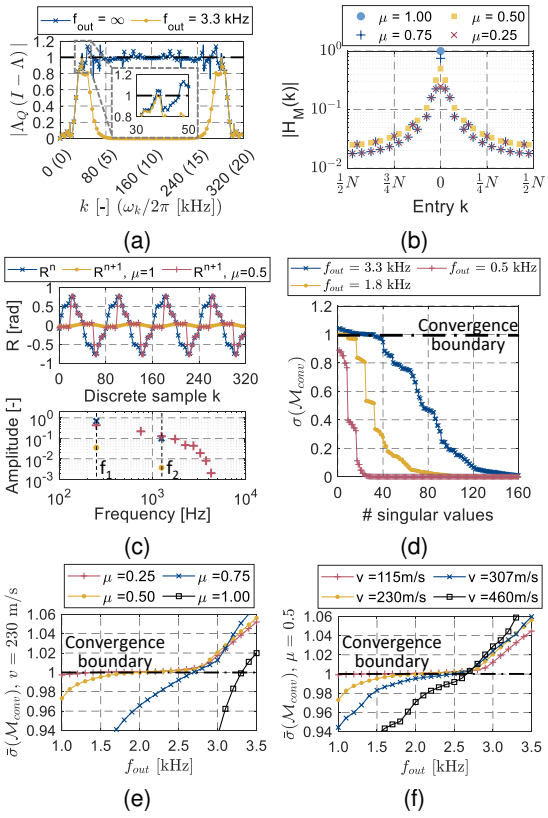

Fig. 7. Convergence analysis of II-AEC. (a) Singular values of $\mathcal{M}_{conv}$ for $\mu = 1$. Learning convergence is ensured with f_{out} =3.3 kHz of Q_{OUT}. (b) $H_M(k)$ for various duty cycles. When $\mu < 1$, Λ_M becomes a circulant matrix, disrupting the frequency alignment between the input and output of the mapping matrix Λ_M. (c) Reference update demonstrates the multi-frequency mapping, where R^n is a dual-sine signal and $Y_\delta = 0$. (d) Largest 160 singular values of $\mathcal{M}_{conv}$ for $\mu = 0.5$. A reduced cut-off frequency f_{out} of Q_{OUT} is necessary to ensure monotonic convergence for the scanning system with $\mu = 0.5$. (e) and (f) Simulation results showing that $\bar{\sigma}(\mathcal{M}_{conv}) < 1$ can be achieved with appropriate f_{out} design for the PM-based SLA under various duty cycles and scan speeds.

Fig. 7(b) shows the middle column of Λ_M for various duty cycles. $H_M(0)$ corresponds to the diagonal entries of Λ_M, indicating the mapping from an input frequency to the same output frequency. The presence of non-zero off-diagonal entries $H_M(k \neq 0)$ in Fig. 7(b) implies that a single input frequency is mapped to multiple output frequencies.

This multi-frequency mapping is demonstrated by comparing the trajectory updates R^n and R^{n+1} from (38), assuming R^n is a dual-sine signal with frequencies $f_1 = 250$ Hz and $f_2 = 1250$ Hz, and $Y_\delta = 0$. The simulation results, presented in Fig. 7(c), show that for $\mu = 1$, the filter $\mathcal{Q}_{OUT}$ with $f_{out} = 3.3$ kHz satisfies (39), reducing the amplitudes of both sinusoidal components in R^{n+1} (yellow dots). However, for $\mu = 0.5$, the original frequencies in R^n are spread into a broader frequency spectrum in R^{n+1} (red crosses), with an increased amplitude at f_2, indicating a violation of (39).

By reducing f_{out}, the monotonic convergence criterion (39) can once again be satisfied for the cascade learning loop, as

Pre-print version of the article: B. Cong, Han Woong Yoo and G. Schitter, "Image Based Iterative Active Error Compensation for Polygon Mirror Based Scanning Systems," *IEEE/ASME Transactions on Mechatronics*pp. 1-12, 2026. DOI: 10.1109/TMECH.2026.3651912

shown in Fig. 7(d). For $f_{out} = 1.8\,\text{kHz}$, the largest singular value is limited to $\bar{\sigma}(\mathcal{M}_{conv}) = 0.9989$. Further reducing f_{out} to 0.5 kHz enhances the learning robustness, though at the expense of learning performance as described in (41).

Fig. 7(e) and 7(f) illustrate that the convergence criterion (39) can be satisfied for the PM-based SLA under different duty cycles and scan speeds. Systems with lower duty cycles require a lower f_{out} to satisfy (39), as a smaller portion of the total FSM dynamics is captured in the images. Conversely, at higher PM speeds, the image-based measurement corresponds to higher-frequency dynamics, allowing a higher f_{out} in the outer loop. For the investigated PM-based SLA, with a duty cycle $\mu = 0.5$ and a scan speed of 230 m/s, the updating filter $\mathcal{Q}_{OUT}$ is chosen with $f_{out} = 1.8\,\text{kHz}$.

The selected filter Q_{IN} guarantees inner-loop convergence with a factor-1.5 robustness margin against multiplicative uncertainties Δ_{IN} of the FSM model [2], defined by

$$P = (1 + \Delta_{IN})\hat{P}. \tag{46}$$

Assessing the robustness of the outer loop is more challenging due to the loss of direct frequency mapping resulting from the duty cycle. Let Δ_{OUT} be defined as the multiplicative uncertainty of the inner-loop dynamic $\mathcal{J}$:

$$\mathcal{J}_\Delta = (I + \Delta_{OUT})\mathcal{J}. \tag{47}$$

Using μ-analysis for ILC [38], it is verified that the chosen $\mathcal{Q}_{OUT}$ achieves robust convergence against 1.5% uncertainty in the range 0-2 kHz and 50% uncertainty in the range 2-10 kHz. Moreover, the singular value comparison in Fig. 7(d) indicates that lowering f_{out} of $\mathcal{Q}_{OUT}$ further improves the outer-loop robustness.

D. Comparison of ILC-AEC and II-AEC

Conventional ILC treats the control reference r as equivalent to the measured output φ', thereby neglecting sensor dynamics in AEC for PM-based scanning systems [2]. This results in a mismatch between r and the true output φ, particularly in high-speed operation, which internal sensing cannot detect and static calibration cannot eliminate. The II-AEC incorporates a dynamic sensor model to reshape the control reference from r to r', thereby compensating for the non-collocation sensing error. It further exploits the correspondence between laser position y and the mirror angle φ to establish an outer loop that eliminates both model and calibration errors. The outer loop operates with the equivalent control reference and measurement pair (y_δ, y_φ).

IV. Experimental Validation

The designed II-AEC is implemented on the PM-based SLA with an inner-loop iteration count $N_m = 19$ and an outer-loop iteration count $N_n = 11$, selected to be sufficiently large for both loops to converge before iteration stops. The achieved performance is evaluated based on the residual cross-scan error and compared to the state-of-the-art ILC-AEC [2].

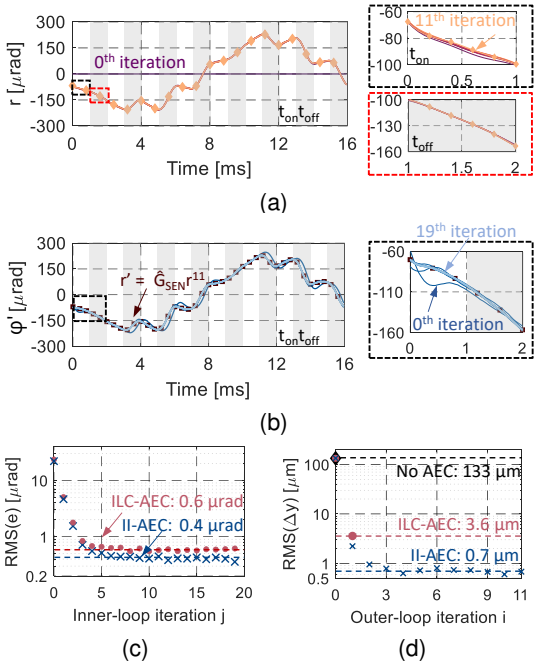

Fig. 8. Learning progress of the II-AEC. (a) Compensation trajectory adapts over 11 iterations. Line brightness indicates the iteration sequence, and the reference r^{11} is marked with diamond markers. (b) Inner-loop iterations with $r' = \hat{G}_{SEN} r^{11}$ (dark red squares) are demonstrated by the evolution of φ' (blue lines), with line brightness indicating the iteration sequence. (c) Inner-loop learning error converges after six iterations and reaches approximately 0.4 μrad. (d) Deterministic cross-scan error reduces from 133 μm to approximately 0.7 μm after three outer-loop iterations of the II-AEC. In comparison, the ILC-AEC reduces the error only to 3.6 μm.

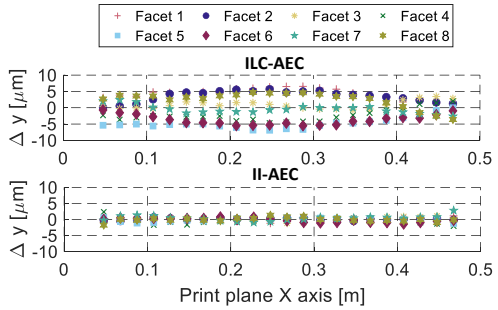

Fig. 9. Measured deterministic cross-scan errors with ILC-AEC (top), and with II-AEC (bottom). Different markers correspond to the PM facets.

A. Cross-scan error reduction with II-AEC

Fig. 8(a) shows the updating progress of the compensation trajectory r in the outer loop. The line color transitions from dark red to light yellow, representing iterations from 0 to 11, while the final trajectory r^{11} is marked with diamonds. Although the trajectory is updated throughout the iterations, the segments corresponding to the t_{off} windows remain nearly unchanged after the initial interpolation in r^1.

The inner-loop iterations for r^{11} are illustrated in Fig. 8(b), where φ' from the FSM internal sensor is plotted against the

Pre-print version of the article: B. Cong, Han Woong Yoo and G. Schitter, "Image Based Iterative Active Error Compensation for Polygon Mirror Based Scanning Systems," *IEEE/ASME Transactions on Mechatronics*pp. 1-12, 2026. DOI: 10.1109/TMECH.2026.3651912

TABLE III
PRINTING PRECISION OF PM-BASED SCANNING SYSTEM

Cross-scan error in RMS	NO AEC [μm]	ILC-AEC [2] [μm]	II-AEC [μm]
Non-deterministic	3.3 µm	3.3 µm	3.3 µm
Deterministic*	133.0 µm	3.6 µm	0.7 µm
Print precision	**133.0 µm**	**4.8 µm**	**3.3 µm**

**Measurement stage precision 0.5 µm (1σ)*

reference $r' = \hat{G}_{SEN} r^{11}$ (marked by squares). From the 0^{th} to the 19^{th} iteration, the tracking signal φ' converges to r', demonstrating successful learning. This learning progress is further confirmed by the root-mean-square (RMS) tracking error in Fig. 8(c), which drops to approximately 0.4 µrad after six inner-loop iterations. The outer-loop learning progress is evaluated based on the deterministic cross-scan error Δy, as shown in Fig. 8(d). The outer loop converges after four iterations, and the learning is stopped after 11 iterations. The RMS deterministic cross-scan error is reduced from an initial 133 µm to approximately 0.7 µm, making the II-AEC over five times more effective than the ILC-AEC and achieving an overall reduction of nearly 200-fold.

In contrast, the ILC-AEC estimates the compensation trajectory from system calibration [2], effectively given by $r = \text{interp1}(t_{on}, L_{OUT}\,\Delta y^0, t_{PM})$. As it does not account for sensor non-collocation, no outer-loop update is performed. For a fair comparison, the ILC-AEC is also iterated until convergence, resulting in a residual tracking error of approximately 0.6 µrad, as shown in Fig. 8(c). This higher error compared to the II-AEC inner loop is attributed to the absence of the filter Q_{OUT} in shaping the trajectory. The ILC-AEC reduces the RMS deterministic cross-scan error to 3.6 µm.

The measured residual cross-scan errors for the cases with ILC-AEC and II-AEC are presented in Fig. 9. Because ILC-AEC does not correct for sensor non-collocation, a significant portion of the deterministic cross-scan error remains due to the internal sensor dynamics of the FSM. II-AEC addresses this issue, resulting in a notable improvement in printing precision across the full scan range.

Tab. III summarizes the printing precision of the PM-based scanning system, evaluated by the RMS of the combined deterministic and non-deterministic cross-scan errors. By implementing II-AEC, the RMS cross-scan error is reduced to 3.3 µm, representing a factor-of-40 improvement compared to the uncompensated system and a 31 % improvement over the ILC-AEC case. After reducing the previously dominant deterministic error, the residual error is primarily due to non-deterministic sources, including 2.2 µm FSM disturbance (measured with the external PSD with the static PM configuration; Fig.4(b)), 0.2 µm frame vibrations (authors' previous work [33]), and possibly 2-5µm PM bearing vibrations [1]. A detailed examination of these sources, while beyond the scope of this study, will be pursued in future work.

B. Print accuracy and uniformity

By moving the Y-stage, a two-dimensional pattern can be printed on the CMOS sensor. Fig. 10(a) shows 'TU WIEN'

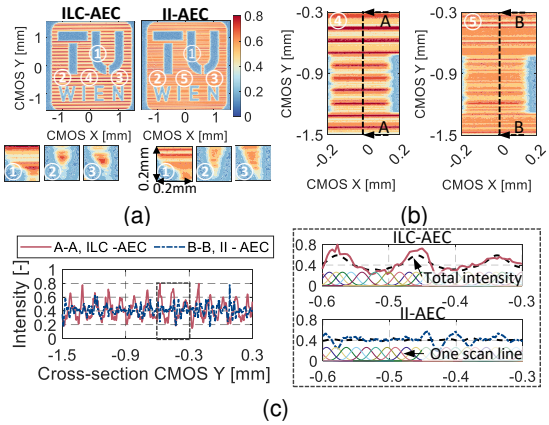

Fig. 10. Print evaluation of the PM-based scanning system. (a) 'TU WIEN' logo is printed on the CMOS sensor at $x = 0.25$ m, with a nominal line-to-line distance of 15 µm in the Y-direction. The prints obtained with ILC-AEC and II-AEC are depicted on the left and right, respectively. (b) Center cuts of the prints highlight the differences in exposure uniformity between the two AEC approaches. (c) Measured exposure intensity profiles along the cross-section are compared with simulated profiles (black dashed lines)

logos printed at $x = 0.25$ m with a line-to-line distance d_{L-L} of 15 µm. The acquired images for both the ILC-AEC (left) and II-AEC (right) cases are shown, with the color bar indicating the normalized exposure energy received by each pixel on the CMOS sensor. Enlarged views of selected areas (① to ③) highlight differences in detail reproduction. While both approaches yield a recognizable reproduction of the target pattern, the II-AEC-enabled system demonstrates superior print accuracy. Specifically, smoother curves in the letter 'U' (①) and sharper peaks in the letters 'W' (②) and 'N' (③) are evident.

In the ILC-AEC-enabled print, a repetitive grid pattern can be observed in the Y-direction, as shown in the zoomed-in view of area ④ in Fig. 10(b). This periodic pattern is less pronounced in the II-AEC case (area ⑤). To quantify this, cross-sectional intensity profiles along sections A-A and B-B are plotted in Fig. 10(c). The standard deviation of the intensity along these cross-sections is $\sigma_{ILC-AEC} = 0.13$ and $\sigma_{II-AEC} = 0.07$ for the ILC-AEC and II-AEC prints, respectively. Simulations of a Gaussian beam scanning in the Y-direction (dashed black lines) confirm that the periodic intensity fluctuations in the ILC-AEC print originate from residual deterministic cross-scan errors. By significantly reducing these errors, II-AEC eliminates the periodic fluctuation, resulting in uniform exposure.

To further evaluate printing quality, single-layer samples were printed using a commercial photosensitive resin (3D Printing UV Sensitive Resin Basic, ANYCUBIC Technology Co., Ltd., Shenzhen, China), following the process described in [2]. 'TU WIEN' logos were printed at three positions along the X-axis ($x = 0.10$, 0.25, and 0.40 m), each measuring 19 mm×15 mm. Figure 11 shows microscopic photos of features corresponding to areas ① and ③, taken in reflected-light mode. With II-AEC, the prints consistently exhibit high feature fidelity across all positions; for example, the sharp peak

Pre-print version of the article: B. Cong, Han Woong Yoo and G. Schitter, "Image Based Iterative Active Error Compensation for Polygon Mirror Based Scanning Systems," *IEEE/ASME Transactions on Mechatronics*pp. 1-12, 2026. DOI: 10.1109/TMECH.2026.3651912

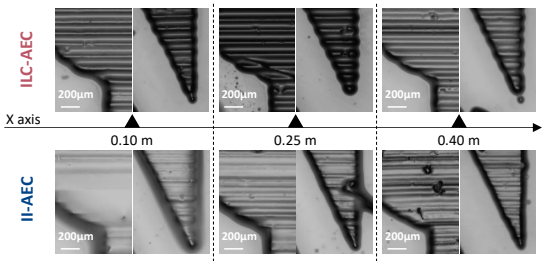

Fig. 11. Single-layer printed samples produced by the PM-based SLA with the ILC-AEC (top) and II-AEC (bottom). The samples are acquired at three representative locations across the scan range. Microscopic photos highlight the detailed print quality for selected regions, focusing on the letters 'U' and 'N' to illustrate fidelity and consistency across the field.

in the letter 'N' remains well-defined. In contrast, the ILC-AEC prints display variability in feature sharpness, indicating inconsistent printing precision.

In the reflected-light images, darker regions correlate with increased surface height variation, as less light is collected by the microscope's objective lens. For prints acquired with the ILC-AEC, the most pronounced surface non-uniformity occurs at the center of the scan range, which reflects the intensity variation measured by the CMOS sensor. By reducing the deterministic cross-scan error, and hence the intensity variation, the II-AEC approach achieves single-layer prints with improved surface uniformity. The remaining surface variation is attributed to non-deterministic cross-scan errors.

C. Discussion

For the PM-based SLA, the proposed II-AEC further advances the state-of-the-art ILC-AEC achieving a printing precision of 3.3 µm and ensuring surface uniformity. However, a key limitation of the II-AEC is its reliance on offline measurements, which confines its corrective capability to deterministic cross-scan errors. Consequently, the achievable precision is ultimately bounded by the system's non-deterministic errors. The residual deterministic error arises from two sources: measurement system inaccuracies and residual learning error. At higher PM operating speeds, the learning bandwidth becomes more limited, which increases the residual learning error and consequently degrades overall scanning precision.

Both iteration loops of the II-AEC are executed offline, and the computational burden is limited to a single linear matrix calculation of size $N \times N$ for each outer- or inner-loop iteration step. The implementation is, however, bottlenecked by data acquisition: each inner-loop iteration takes a few seconds, whereas each outer-loop iteration takes approximately 1.2 hours. This duration is dominated by repeated image captures at multiple locations needed to extract deterministic scan-line positions with high precision. Using multiple imaging sensors or faster laser-position measurement hardware, such as a PSD, could reduce the outer-loop iteration time to a few minutes, thereby improving the practicality of II-AEC for routine or periodic calibration in PM-based scanning systems.

In summary, an image-based iterative active error compensation for a polygon mirror-based stereolithography system has been designed and implemented, achieving uniform and precise printing at high speeds. The performance is demonstrated by projecting images on a CMOS sensor and printing single-layer samples on photosensitive resin.

V. Conclusion

In this paper, image-based iterative active error compensation is proposed for polygon mirror-based scanning systems, improving printing precision and uniformity. The AEC uses an FSM to reduce deterministic cross-scan errors of the scanning system but suffers from sensor non-collocation errors, causing FSM angle deviations and resulting in imperfect compensation. These angle deviations can be evaluated using position measurements of the scanning laser and added to FSM control. However, this introduces non-linearity in the control loop due to the time-varying gain and duty cycle associated with the PM-based scanning system. The II-AEC tackles this challenge with cascade learning control, where the learning and updating filters are designed to balance learning convergence and performance. By implementing the II-AEC in a PM-based SLA, the deterministic cross-scan error is reduced to 0.7 µm from the initial 133.0 µm. The SLA with II-AEC achieves a printing precision of 3.3 µm, equivalent to a 40-fold improvement compared to the uncompensated SLA, advancing the state-of-the-art ILC-AEC by another 30%. The precision improvement is demonstrated by pattern projection on CMOS sensors and high-fidelity single-layer resin prints.

Beyond SLA, the proposed II-AEC can be integrated as a calibration procedure to a wide range of applications that utilize PM-based scanners, such as laser machining, LiDAR, and scanning microscope, where enhanced scanning accuracy is necessary. Furthermore, the image-based learning algorithm underlying II-AEC can be extended to other scanner types, such as galvanometer scanners, which face similar challenges, including sensor non-collocation and limited duty cycles.

References

[1] G. F. Marshall and G. E. Stutz, *Handbook of Optical and Laser Scanning*. CRC Press, oct 2018.
[2] B. Cong, H. W. Yoo, D. Pechgraber, and G. Schitter, "High-speed and high-resolution polygon mirror-based industrial stereolithography with advanced active error compensation," *IEEE/ASME Trans. Mechatron.*, pp. 1–10, 2025.
[3] M. N. Sweeney, G. A. Rynkowski, M. Ketabchi, and R. Crowley, "Design considerations for fast-steering mirrors (FSMs)," in *Proc. SPIE*, S. F. Sagan, G. F. Marshall, and L. Beiser, Eds. SPIE, jun 2002.
[4] E. Csencsics and G. Schitter, "Exploring the pareto fronts of actuation technologies for high performance mechatronic systems," *IEEE/ASME Trans. Mechatronics*, vol. 26, no. 2, pp. 1053–1063, apr 2021.
[5] R. P. Aylward, "Advances and technologies of galvanometer-based optical scanners," in *Optical Scanning: Design and Application*, L. Beiser, S. F. Sagan, and G. F. Marshall, Eds. SPIE, jul 1999.
[6] B. Cong, J. Schlarp, and G. Schitter, "Iterative learning control for the active error correction of polygon mirror based laser scanning," in *IEEE/ASME Int. Conf. Adv. Intell. Mechatron. AIM*. IEEE, jul 2022.
[7] J. M. Hilkert, G. Kanga, and K. Kinnear, "Line-of-sight kinematics and corrections for fast-steering mirrors used in precision pointing and tracking systems," in *Proc. SPIE*, D. J. Henry, D. A. Lange, D. Linne von Berg, S. D. Rajan, T. J. Walls, and D. L. Young, Eds., vol. 9076. SPIE, Jun. 2014, p. 90760F.
[8] L. Wang, X. Liu, and C. Wang, "Modeling and design of fast steering mirror in image motion compensation for backscanning step and stare imaging systems," *Opt. Eng.*, vol. 58, no. 10, p. 1, Oct. 2019.

Pre-print version of the article: B. Cong, Han Woong Yoo and G. Schitter, "Image Based Iterative Active Error Compensation for Polygon Mirror Based Scanning Systems," *IEEE/ASME Transactions on Mechatronics* pp. 1-12, 2026. DOI: 10.1109/TMECH.2026.3651912

[9] J. Schlarp, E. Csencsics, and G. Schitter, "Optical scanning of a laser triangulation sensor for 3-d imaging," *IEEE Trans. Instrum. Meas.*, vol. 69, no. 6, pp. 3606–3613, Jun. 2020.
[10] D. J. Kluk, M. T. Boulet, and D. L. Trumper, "A high-bandwidth, high-precision, two-axis steering mirror with moving iron actuator," *Mechatronics*, vol. 22, no. 3, pp. 257–270, Apr. 2012.
[11] L. E. Hawe, "Control of a fast steering mirror for laser-based satellite communication," Doctoral dissertation, Massachusetts Institute of Technology, 2006.
[12] R. Xiao, M. Xu, S. Shao, and Z. Tian, "Design and wide-bandwidth control of large aperture fast steering mirror with integrated-sensing unit," *Mech. Syst. Signal Process.*, vol. 126, pp. 211–226, Jul. 2019.
[13] S. Ito, E. Csencsics, and G. Schitter, "Modeling-free learning control of cross-coupled fast steering mirror for 2-d trajectory," *IFAC-PapersOnLine*, vol. 56, no. 2, pp. 5340–5345, 2023.
[14] E. Csencsics and G. Schitter, "System design and control of a resonant fast steering mirror for lissajous-based scanning," *IEEE/ASME Trans. Mechatron.*, vol. 22, no. 5, pp. 1963–1972, oct 2017.
[15] H. W. Yoo, S. Ito, M. Verhaegen, and G. Schitter, "Transformation-based iterative learning control for non-collocated sensing of a galvanometer scanner," in *Eur. Control Conf. (ECC) 2013*. IEEE, Jul. 2013, pp. 1204–1209.
[16] J. G. Garcia, L. A. Sievers, and A. von Flotow, "High-bandwidth positioning control of small payloads mounted on a flexible structure," *J. Guid. Control Dyn.*, vol. 15, no. 4, pp. 928–934, Jul. 1992.
[17] D. M. Southwood, "Ccd-based optical tracking loop design trades," in *Proc. SPIE*, D. L. Begley and B. D. Seery, Eds., vol. 1635. SPIE, Jun. 1992, p. 286.
[18] T. Tang, S. Niu, J. Ma, B. Qi, G. Ren, and Y. Huang, "A review on control methodologies of disturbance rejections in optical telescope," *Opto-Electron. Adv.*, vol. 2, no. 10, p. 190011, 2019.
[19] J. Klotz, M. Gupta, and A. C. Sankaranarayanan, "Computational 3d imaging with position sensors," in *Proc. IEEE/CVF Int. Conf. Comput. Vis. (ICCV)*. IEEE, Oct. 2023, pp. 8091–8100.
[20] M. J. Kay, A. A. Rakhman, and S. M. Cousineau, "Active pointing control of pulsed, high-power laser beam after 65-meter transport," in *Proc. IEEE Int. Conf. Control Autom. (ICCA)*. IEEE, Jun. 2022, pp. 565–570.
[21] J. Keaveney, "Automated translating beam profiler for in situ laser beam spot-size and focal position measurements," *Rev. Sci. Instrum.*, vol. 89, no. 3, Mar. 2018.
[22] C.-F. Ding, M.-S. Lee, and K.-M. Li, "Development of on-line laser power monitoring system," in *Proc. SPIE Real-Time Meas., Rogue Events, Emerg. Appl.*, B. Jalali, S. K. Turitsyn, D. R. Solli, and J. M. Dudley, Eds., vol. 9732. SPIE, Mar. 2016, p. 97320T.
[23] A. Virto, I. Vila, T. Rodrigo, F. Matorras, C. Figueroa, E. Calvo, A. Calderón, P. Arce, J. Oller, A. Molinero, M. Josa, A. Ferrando, M. Fernández, and J. Barcala, "Study of cmos image sensors for laser beam position detection," *Nucl. Instrum. Methods Phys. Res. A*, vol. 497, no. 2-3, pp. 397–406, 2003.
[24] M. Šarbort, Š. Rerucha, P. Jedlicka, J. Lazar, and O. Cíp, "Tilt angle measurement with a gaussian-shaped laser beam tracking," in *Opt. Micro- Nanometrol. V*, C. Gorecki, A. K. Asundi, and W. Osten, Eds., vol. 9132. SPIE, May 2014, p. 91321E.
[25] K. Hashimoto, "A review on vision-based control of robot manipulators," *Adv. Robot.*, vol. 17, no. 10, pp. 969–991, Jan. 2003.
[26] A. P. Dani, *Image-Based Estimation for Robotics and Autonomous Systems*. Springer International Publishing, 2021, pp. 963–967.
[27] P. C. Marchal, O. Sörnmo, B. Olofsson, A. Robertsson, J. G. Ortega, and R. Johansson, "Iterative learning control for machining with industrial robots," *IFAC Proc. Vol.*, vol. 47, no. 3, pp. 9327–9333, 2014.
[28] D. J. Hoelzle, A. G. Alleyne, and A. J. Wagoner Johnson, "Iterative learning control for robotic deposition using machine vision," in *Am. Control Conf. (ACC)*. IEEE, Jun. 2008, pp. 4541–4547.
[29] E. Tureyen, Y. Karpat, and M. Cakmakci, "Development of an iterative learning controller for polymer based micro-stereolithography prototyping systems," in *Am. Control Conf. (ACC)*. IEEE, Jul. 2016, pp. 852–857.
[30] D. Shen, "Iterative learning control with incomplete information: a survey," *IEEE/CAA J. Autom. Sin.*, vol. 5, pp. 885–901, Sep. 2018.
[31] H.-S. Ahn, K. L. Moore, and Y. Chen, "Discrete-time intermittent iterative learning controller with independent data dropouts," *IFAC Proc. Vol.*, vol. 41, no. 2, pp. 12 442–12 447, 2008.
[32] S. Hager, E. Csencsics, H. W. Yoo, and G. Schitter, "Reducing the uncertainty of laser straightness measurements via local saturation of imaging sensors," in *IEEE/ASME Int. Conf. Adv. Intell. Mechatron. AIM*. IEEE, Jul. 2024, pp. 1567–1572.
[33] B. Cong, H. W. Yoo, D. Pechgraber, and G. Schitter, "Cross-scan error evaluation of large size polygon mirror based laser scanning system for industrial 3d printing," in *IEEE/ASME Int. Conf. Adv. Intell. Mechatron. AIM*. IEEE, Jul. 2024, pp. 290–295.
[34] J. H. Burge, "An easy way to relate optical element motion to system pointing stability," in *Current Developments in Lens Design and Optical Engineering VII*. SPIE, Aug. 2006, p. 18.
[35] Y. Li, "Laser beam scanning by rotary mirrors ii conic-section scan patterns," *Applied Optics*, vol. 34, no. 28, p. 6417, Oct. 1995.
[36] G. Pipeleers and K. L. Moore, "Unified analysis of iterative learning and repetitive controllers in trial domain," *IEEE Trans. Autom. Control.*, vol. 59, no. 4, pp. 953–965, Apr. 2014.
[37] R. M. Gray, "Toeplitz and circulant matrices: A review," *Found. Trends Commun. Inf. Theory.*, vol. 2, no. 3, pp. 155–239, 2005.
[38] T. Donkers, J. van de Wijdeven, and O. Bosgra, "Robustness against model uncertainties of norm optimal iterative learning control," in *Amer. Control Conf. (ACC) 2008*. IEEE, Jun. 2008, pp. 4561–4566.
[39] K. L. Moore, *Iterative learning control for deterministic systems*. Springer Science & Business Media, 2012.

Bo Cong received the M.Sc. degree in mechanical engineering from the Eindhoven University of Technology (TU/e), Eindhoven, Netherlands, in 2017.

He is currently a Doctoral Researcher at the Mechatronics and Power Electronics Institute (MPEI), TU Wien, Vienna, Austria. His main research interests include precision engineering in mechatronic and optomechatronic systems, active vibration isolation, and advanced control design for linear systems.

Han Woong Yoo (Member, IEEE) received the B.Sc. degree in electrical and electronics engineering from Yonsei University, Seoul, South Korea, the M.Sc. degree in electrical engineering from Seoul National University, Seoul, in 2007, and the Ph.D. degree in optomechatronics and adaptive optics for confocal microscopy from the Delft University of Technology, Delft, Netherlands, in 2015.

He worked with the Samsung Advanced Institute of Technology (SAIT) and Samsung Electronics Company Ltd., semiconductor business, for low-power digital RF and algorithms for reliability of multilevel nonvolatile memories. He is currently a Postdoctoral Researcher at the Advanced Mechatronic Systems group at the Mechatronics and Power Electronics Institute (MPEI), TU Wien, Vienna, Austria. His main research interests include optical metrology, precision mechatronics systems, and biomedical imaging.

Georg Schitter received the M.Sc. degree in electrical engineering from TU Graz, Graz, Austria, in 2000, and the M.Sc. degree in information technology, and the Ph.D. degree in technical sciences from ETH Zurich, Zurich, Switzerland, in 2004. He is currently the department head and a professor at the Mechatronics and Power Electronics Institute (MPEI), TU Wien, Vienna, Austria. His main research interests include highper formance mechatronic systems, particularly for applications in the high-tech industry, scientific instrumentation, and mechatronic imaging systems, such as AFM, scanning laser and LIDAR systems, telescope systems, adaptive optics, and lithography systems for semiconductor industry.

Dr. Schitter was the recipient of the journal Best Paper Award of IEEE/ASME TRANSACTIONS ON MECHATRONICS (2018), of the IFAC Mechatronics (2008-2010), of the Asian Journal of Control (2004-2005), and the 2013 IFAC Mechatronics Young Researcher Award. He served as an Associate Editor for IFAC Mechatronics, Control Engineering Practice, and for IEEE TRANSACTIONS ON MECHATRONICS.

Pre-print version of the article: B. Cong, Han Woong Yoo and G. Schitter, "Image Based Iterative Active Error Compensation for Polygon Mirror Based Scanning Systems," *IEEE/ASME Transactions on Mechatronics*pp. 1-12, 2026. DOI: 10.1109/TMECH.2026.3651912